Volume 1 | Number 1 | Jan 2013 | Pages 1–100

PCCP

Physical Chemistry Chemical Physics
www.rsc.org/pccp

ROYAL SOCIETY OF CHEMISTRY

ROYAL SOCIETY OF CHEMISTRY

www.rsc.org/pccp

PCCP

PAPER

Interplay of chemical structure and magnetic order coupling at the interface between Cr_2O_3 and Fe_3O_4 in Hybrid Nanocomposites

Ruth Otero-Lorenzo,[a] Mads C. Weber,[a,b] Pamela A. Thomas,[c] Jens Kreisel[b] and Verónica Salgueiriño[a*]

Hybrid nanocomposites based on ferrimagnetic (FiM) Fe_3O_4 and magnetoelectric antiferromagnetic (AFM) Cr_2O_3 nanocrystals were synthesized to offer a particular three-dimensional (3D) interface between the two oxides. This interface favours an intermixing process (demonstrated combining Raman spectroscopy and magnetization measurements) that determines the final magnetic behavior.

Introduction

10 Heterostructures of transition metal oxides can offer particularly interesting interfaces by down sizing the nanocrystals forming them. This interface is characterized by an energetic change that can become not nullified but reduced by local 15 relaxation related to processes of diffusion and chemical ion redistribution.[1] The correlation between chemical composition and structure considering the particularities of the nanoscale systems, taking into account ion and vacancy diffusion lengths, becomes therefore an important dynamical variable to control the 20 final properties of nanostructures characterized by the interface, for example in nanocomposites. For example, changes in the cationic valence state associated with changes in oxygen vacancy concentration profoundly affect magnetic, electronic and transport properties.[2] Accordingly, developments in the synthetic 25 approaches to exploit and control the different mobility of cations and anions to engineer gradients in static and dynamic chemistry and carrier concentrations will be very convenient.[3] Beberwyck *et al.* have recently highlighted postsynthetic modifications of preformed nanostructures for the construction of complex 30 nanomaterials exploiting cation exchange reactions.[4] The interfaces established in this way offer a combination of effects depending on the local chemical composition, the crystallographic orientation, the type of coupling, and/or the 3D connectivity pattern between the transition metal oxide 35 nanocrystals. As a result, the heterostructures allow therefore enhanced and/or diversified capabilities,[5] depending on the lattice, electronic and orbital reconstruction at the interfaces.[6] For that reason, the complete characterization of hybrid nanocomposites requires a combination of techniques such that 40 the contributions from individual components and from the density of the interfaces established can be uniquely described.

Herein, we report nanoparticulated composites based on ferrimagnetic (FiM) (and multiferroic at low temperatures) Fe_3O_4 and magnetoelectric and antiferromagnetic (AFM) Cr_2O_3. The 45 particular three-dimensional (3D) interface established between

the nanoparticles of the two oxides favours an intermixing process, which determines the interplay between chemical structure and magnetism.

Experimental section

50 Chromium oxide nanoparticles were synthesized by means of a controlled precipitation of $Cr(OH)_3$ in basic medium.[7] Accordingly, 5 mL of $Cr(NO_3)_3$ (0.1 M (Aldrich)) is added dropwise under mechanical stirring to 5 mL of NaOH (0.3 M (Aldrich)). Once the nanoparticles are formed, they are 55 centrifuged, washed and annealed at 800ºC in air to promote the formation of the chromium oxide. $Fe_3O_4 – Cr_2O_3$ nanocomposites synthesis was carried out according to the modification of a previous method reported to produce Fe_3O_4 nanoclusters.[8] $FeCl_3$ (5 mmol (Fluka)) was dissolved in ethylene glycol (40 mL 60 (Aldrich)), followed by addition of NaAc (3.6 g (Aldrich)) and polyethylene glycol (1.0 g (Aldrich)), in the presence of the Cr_2O_3 (0.76 mg) nanoparticles previously synthesized. The mixture was stirred for 30 min and sealed in a teflonlined stainless-steel autoclave, heated to and maintained at 185 ºC for 8 65 h, and then allowed to cool down. The black products were washed and dried.

The samples were characterized by transmission electron microscopy (TEM), performed on a JEOL JEM1010 instrument operating at an acceleration voltage of 100 kV. High resolution 70 (HR) and high-angle annular dark-field scanning TEM (HAADF-STEM) and energy dispersive x-ray elemental analyses (EDS) were carried out on a field emission JEOL JEM2010F working at 200 kV. Samples for TEM and HRTEM analysis were prepared by dropping a diluted suspension of the nanocomposites onto an 75 ultrathin carbon coated copper grid. X-ray diffraction patterns were collected using a Siemens D-5000 powder X-ray diffractometer (Cu K_α radiation (λ = 1.54056 Å) in the 10-90º 2θ range) and compared with crystallographic information files (CIF) from the crystallographic open database (COD). Raman 80 spectra were collected with a Renishaw in Via Reflex Raman Microscope. Experiments were conducted at room temperature

using three different excitation wavelengths: a red 633 nm line from a HeNe laser, a green 514 nm line form an Argon laser and a blue 442 nm line from a HeCd laser with a spectral cut-off of at about 120 cm^{-1}. Magnetic measurements were performed using a Quantum Design MPMS XL7 SQUID Magnetometer.

Results and Discussion

The hybrid nanocomposites were synthesized using a solvothermal method in which the reaction mechanism is described as a two-stage growth process in which primary nanocrystals of Fe_3O_4 nucleate first and then aggregate uniformly into larger secondary structures,[8] though in this case, in the presence of Cr_2O_3 nanoparticles, previously synthesized.[7] The method offers increased amounts of the nanocomposites, implying therefore advantages in terms low-cost production and up-scaling possibilities. The characterization of the as-synthesized heterostructures was performed focusing on size, crystallinity and composition. Figure 1a shows the $Fe_3O_4 - Cr_2O_3$ nanocomposites, with an average diameter of 172 ± 24 nm (Gaussian analysis). HR-TEM (figure 1b) resolves the individual smaller units forming the composites and HAADF-STEM in combination with STEM-XEDS element mapping shown in figure 1c and d demonstrates the hybrid morphology. Figure 1c reflects the relative distribution of the metallic elements, with red and green areas corresponding to Cr and Fe, respectively, and underlines the random distribution of the two oxides forming the heterostructures. The Cr_2O_3 nanoparticles (~35 wt.%) in the final composites have an average diameter of 51 ± 16 nm average diameter; Fe_3O_4 units (~ 65 wt.%) are smaller with a ~10 nm average diameter. Since the TEM images shown do not allow distinguishing the individual Fe_3O_4 nanoparticles, we have considered dark-field STEM images for their size distribution analysis.
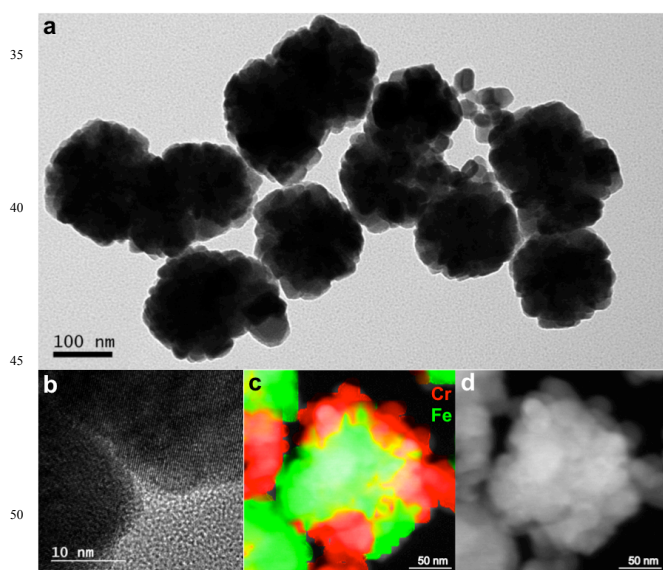

Figure 1. TEM (a), HRTEM (b) and HAADF-STEM images (c and d) and EDS elemental mappings (in c) showing the distribution of the Cr (red) and Fe (green) within the nanocomposites.

The X-ray diffraction (XRD) pattern of the $Fe_3O_4 - Cr_2O_3$ composites (in black), with the reference patterns of magnetite (Fe_3O_4, red, ref.: JPCDS-ICDD card 10-0319) and eskolaite (Cr_2O_3, green, ref.: JPCDS-ICDD card 38-1479) are given in figure 2. Even though the units forming the composites are rather small (down to ~10 nm in case of the Fe_3O_4) and randomly orientated, as checked by TEM, it is possible to resolve the diffraction pattern. Comparison of the diffraction pattern of the composites to the references illustrates that the sample corresponds to Cr_2O_3 and Fe_3O_4 as main components and enables to assign the intensities to diffracting planes of both oxides. The direct contact between oxides implies gradients of chemical potential that promote intermixing processes, favoring the formation of the mixed chromium-iron oxides such as $Cr_{2-x}Fe_xO_3$ and $Fe(Fe_{2-x}Cr_x)O_4$, considering the flow of Cr^{3+} ions to the magnetite phase and the flow of Fe^{3+} ions to the eskolaite phase. Indeed, kinetic factors become key in determining the feasibility of an ion exchange reaction, especially at the nanoscale at which limits of long-range solid-state ion diffusion are significantly relaxed by the large surface-to-volume ratios.[4] The composites offer indeed such situation, which becomes rather favored considering the morphology attained by the heterostructures with the 3D connectivity pattern between both oxides. We can however discard the formation of a mixed ferrite ($CrFe_2O_4$) considering a redox process to obtain Cr^{2+} from Cr^{3+} and Fe^{3+} from Fe^{2+} ions, given the standard reduction potentials.
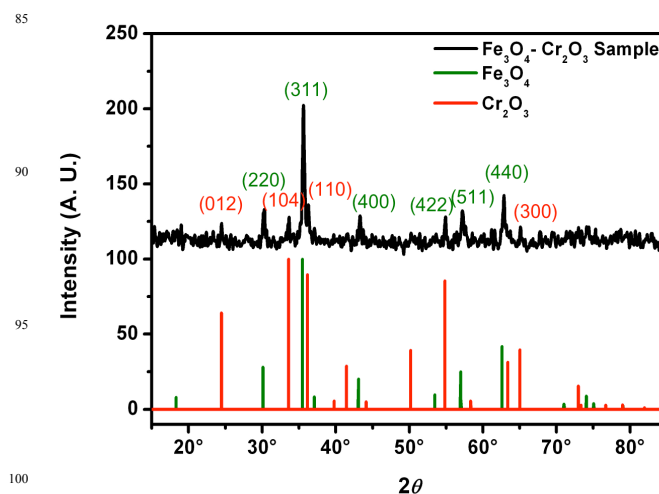

Figure 2. XRD pattern of the $Fe_3O_4 - Cr_2O_3$ sample (black) compared to reference patterns of magnetite (green) and eskolaite (red).

Raman spectroscopy is a powerful probe for investigating vibrational and structural properties of materials[9] and can provide unique information for analyzing hybrid structures that combine several transition metal oxides. However, the power from a laser excitation source can lead in transition metal oxides to local heating in Raman experiments, especially when the laser beam is focused to a small spot size.[10-12] With this into account, we have carefully checked (for the three wavelengths employed) not to heat the sample in order to avoid modifications of the spectral signature. Additionally, considering the fact of studying hybrid

nanocomposites, we have first verified the reproducibility of spectra on different places of the sample. Figure S1 includes the Raman spectra of the sample containing the hybrid nanostructures as dried powder, collected at room temperature and in three different spots. The consistence of the different spectra obtained with a 1µm laser spot reflects the homogeneity of the sample on a micrometer scale.

Though already routinely applied to thin films, Raman spectroscopy is less (but increasingly) used to characterize heterostructured and/or nanoparticulate-based materials.[13-16] Furthermore, the vast majority of Raman studies on oxides uses a single wavelength only, which is selected according to the best Raman signal or to reduce the substrate background signal and fluorescence. Here, we have employed different laser wavelengths for the investigation of the hybrid nanostructures, to allow differentiating the singular parts of the nanocomposites. Figure 3a shows room temperature Raman spectra obtained for three different excitation wavelengths (442, 514 and 633 nm). The spectra consist of both broad features (for example between 580 cm^{-1} and 760 cm^{-1} or between 260 cm^{-1} and 420 cm^{-1}, due to overlapping bands) and rather defined bands like the modes at 550 cm^{-1} or at 675 cm^{-1} when excited with the red laser. Although the spectra of different wavelengths are similar at first sight, a closer inspection reveals the spectra present different features for different wavelengths. For understanding such dissimilar features three different but linked factors shall be considered; a) the optical confocal depth, that decreases with decreasing wavelength for a given material, b) absorption, since a decrease in the laser wavelength can lead to an increase in absorption and consequent reduction of the penetration depth, and c) Raman cross section, the Raman intensity of a given material, depending on the exciting wavelength can lead to resonant Raman effects.[13]

In order to assign the different spectral features of the hybrid nanocomposites in figure 3a, we discuss their different signatures by comparing the spectra to data from the literature for the oxides the nanocomposites consist of;[10,16-20] the main compounds eskolaite (Cr_2O_3) and the magnetite (Fe_3O_4). We also take into account the spectra of the Cr_2O_3 nanoparticles previously synthesized and used to later include in the nanocomposites and of Fe_3O_4 nanocomposites (synthesized following the same method as the one herein reported, but in the absence of the chromium oxide nanoparticles) (see figures S2 and S3 in the supporting information (SI)). Additionally, we have to consider the mixed oxides mentioned before ($Cr_{2-x}Fe_xO_3$ and $Fe(Fe_{2-x}Cr_x)O_4$) as well as the possible formation of hematite (α-Fe_2O_3) and maghemite (γ-Fe_2O_3), especially at the interface between nanoparticles and at the surface of the outer nanoparticles in the composites (where an oxidation process is more favored).

Let us first recall the main feature of the spectral signatures of potentially present materials. Fe_3O_4 crystallizes in the *Fd3m* space group which gives rise to five Raman active modes $\Gamma = A_g + E_g + 3T_{2g}$. Seven Raman active modes, $\Gamma = 2A_{1g} + 5E_g$, have been predicted by group theory for the *R-3c* crystal structure of Cr_2O_3 as well as for the potentially formed α-Fe_2O_3. All possible modes have been observed in single crystal Raman spectroscopy measurements and reported by Hart *et al.* including mode assignment to the appropriate vibration symmetry.[17-19] In the case of Fe_3O_4, the main features appear at 675 cm^{-1} (A_{1g}) and 550 cm^{-1}

(T_{2g}), though the A_{1g} mode is by far stronger than the T_{2g} mode. The Raman spectrum of Cr_2O_3 is dominated by a very intense mode A_{1g} at 553 cm^{-1} (see figures S2 and S3 in the SI). The bands of highest intensity of α-Fe_2O_3 can be found in the rather low energy region around 230 cm^{-1} (A_{1g}), 253 cm^{-1} (E_g), 298 cm^{-1} (E_g + E_g). The spectrum of γ-Fe_2O_3 on the other hand shows rather broad features between 300 cm^{-1} and 400 cm^{-1}, 425 cm^{-1} and 540 cm^{-1} as well as 600 cm^{-1} and 750 cm^{-1}.[10] Main mode bands appear marked in pale pink (Fe_3O_4), in pale green (Cr_2O_3), in pale blue (γ-Fe_2O_3), and in pale grey areas (α-Fe_2O_3) in the graphs in figure 3.
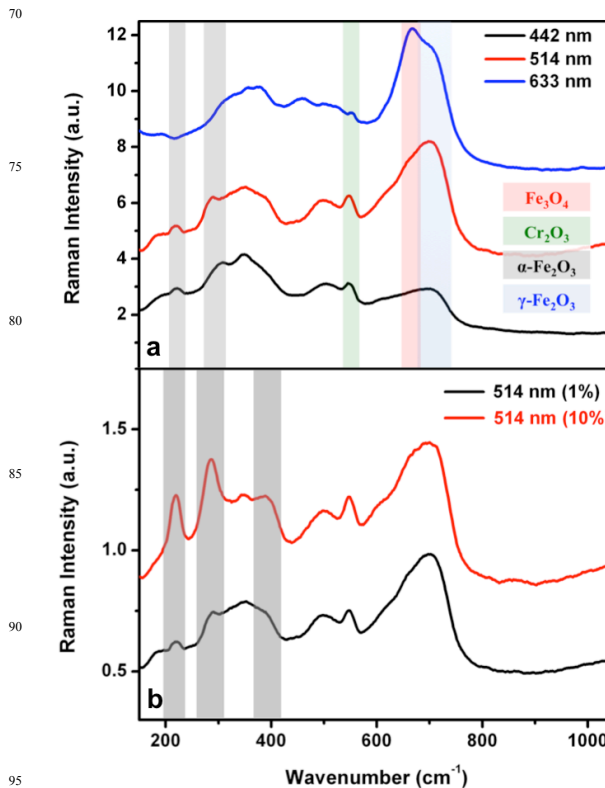

Figure 3. (a) Comparisons of the Raman spectra from the Fe_3O_4 – Cr_2O_3 heterostructures obtained at different excitation wavelengths (442, 514 and 633 nm). (b) Comparison of the Raman spectra obtained using different density of power (at 1 and 10%) from the laser excitation source (514 nm).

Having considered these most dominant features, all spectra show broad bands in the regions of 350 cm^{-1}, 500 cm^{-1} and 700 cm^{-1}, which reflect spectral signatures of maghemite (γ-Fe_2O_3) though the asymmetric shape and the high intensity of the feature between 580 cm^{-1} and 760 cm^{-1} suggests that this region cannot only be explained by the presence of this iron oxide. McCarty and Boehme reported a study on $Cr_{2-x}Fe_xO_3$ and $Fe(Fe_{2-x}Cr_x)O_4$ solid solutions.[20] The main feature of both solid solutions systems was found in the region of 600 cm^{-1} and 720 cm^{-1} with an asymmetric deformation towards smaller wavenumbers due to several close bands and accordingly, the solid solutions of the iron and chromium oxides strongly contribute to the feature located around 700 cm^{-1}. On the other hand we can appreciate that the excitation with the red laser leads to a change of the shape of this

feature, when compared with spectra under excitation of the blue and green lasers, now dominated by a rather sharp band at around 675 cm^{-1}, which can be assigned to the strongest band in Fe_3O_4. Another well-defined band peaks at 550 cm^{-1} where both Fe_3O_4
5 and Cr_2O_3 have a vibration mode. This band is visible throughout all the spectra of different laser wavelength whereas the band at 675 cm^{-1} of Fe_3O_4, which is the most dominant band of Fe_3O_4, can only be detected under excitation with the 633 nm laser. Therefore we assign the feature at 550 cm^{-1} as one of the A_{1g}
10 modes of the Cr_2O_3 component of the nanocomposites. The observed changes in intensity of the Raman spectra under excitation of different wavelength, which enable especially the identification of the Cr_2O_3 and Fe_3O_4 phases, are due to different electronic structures and thus different resonant and absorption
15 effects of these oxides. We note that the presence of mixed iron-chromium oxides as well as potential contributions from binary oxides is not surprising as they are expected to form the interface of Fe_3O_4 and Cr_2O_3. On the other hand, after such investigation with well-controlled laser power, we have also intentionally used
20 higher laser power to test the effect of heating on our nanocomposites (figure 3b). Significant modifications, namely an intensity enhancement around 220, 300 and 400 cm^{-1}, suggest a markedly increased proportion of α-Fe_2O_3.[10,12] However, a detailed investigation of this heating induced transformation and
25 the likely impact on the coupling properties is beyond the scope of this publication.

　　The magnetic properties of the hybrid nanocomposites were recorded using a superconducting quantum interference device (SQUID) magnetometer at different temperatures and were
30 examined in terms of magnetization, coercivity and exchange bias. The MvsH curves (figure 4a and b) of the sample display open hysteresis loops in all the temperatures considered, even at 295 K. Instead of the typical superparamagnetic behavior expected for the Fe_3O_4 and Cr_2O_3 nanoparticles with close
35 hysteresis loops, we can observe a blocked-like state due to the important interactions established in the sample, due to nanoparticle and nanocomposite interactions. Independently of their different magnetic order, the FiM magnetite and the AFM Cr_2O_3 nanoparticles are expected to present a superparamagnetic
40 behavior. In the case of the ~10 nm Fe_3O_4 nanoparticles, all the atomic magnetic moments become coupled to coherently fluctuate at room temperature as a one large nanoparticle magnetic moment.[21] In the case of the Cr_2O_3, since AFM, we have to consider only the atomic magnetic moments from the
45 surface giving a paramagnetic contribution. Indeed, nanoparticles of AFM materials have non-zero magnetic moments and are therefore, strictly speaking, not AFM.[22-25] Numerous magnetization studies of AFM nanoparticles have shown that both the initial susceptibility and the magnetization in large
50 applied fields are considerably larger than in the corresponding bulk materials. Néel justified this result due to the finite number of magnetic atoms in the nanoparticles, which may lead to a difference in the numbers of spins in the two sublattices because of random occupancy of lattice sites.[26] This results in an
55 uncompensated magnetic moment μ, which in the case of AFM nanostructures without impurities either of FM or FiM materials, comes from a random occupation of surface sites. On the other hand, the magnetoelectric AFM materials, like Cr_2O_3, have an

equilibrium boundary polarization, which is coupled to the bulk
60 AFM order parameter. This boundary polarization, roughness insensitive, has been demonstrated to contribute to the magnetization.[27,28]
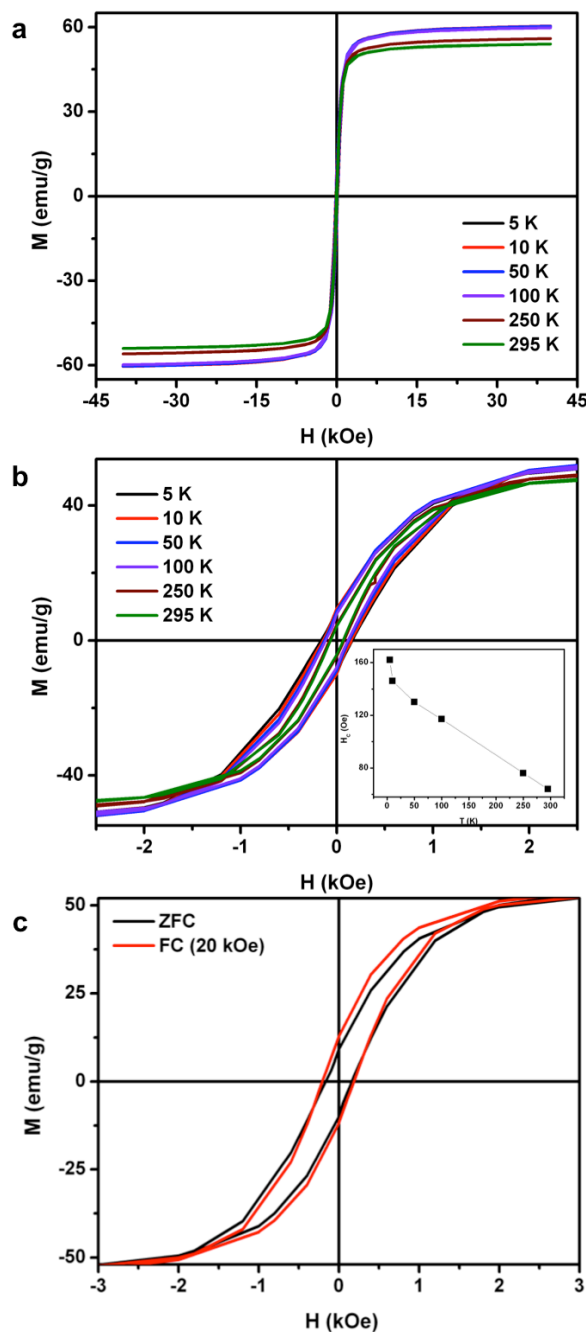

Figure 4. Hysteresis loops of the hybrid nanocomposites recorded at different temperatures (a), hysteresis loops at low fields (b) and
110 hysteresis loops at 5K after zero-field cooling and field-cooling (20 kOe) (c).

　　Accordingly, the hysteresis loops included in figure 4 can be associated to these two main contributions; one responsible for
115 the large magnetization values due to the ferrimagnetic (FiM) magnetite　　　nanoparticles,　　　which　　　superimposes　　　the

antiferromagnetic contribution responsible for the subtle slope and almost non-saturation of the magnetization at high field values, that corresponds to the chromium oxide magnetic phase identified. Figure S4 (in the SI) includes the hysteresis loops collected at 10 K of two samples of magnetite nanocomposites (normalized on the graph on the right), synthesized in the absence and presence of Cr_2O_3 nanoparticles. From these graphs, it is clear that the magnetite-based sample reaches larger values of magnetization at much lower magnetic fields. The sample with the two oxides, the Fe_3O_4-Cr_2O_3 nanocomposites, shows lower values of magne-tization and needs larger applied magnetic fields (due to the AFM chromium oxide). At 10 K (as shown in this graph in figure S4, the magnetite-based sample reaches a $M_S = 80$ emu/g (~ 80% of the M_S value measured by Smit and Wijn for bulk[29]). The Fe_3O_4-Cr_2O_3 nanocomposites on the contrary, because of the AFM chromium oxide, reaches a $M_S = 60$ emu/g.

The configuration or disposition of the nanoparticles, randomly assembled and coupled in the nanocomposites justifies the non-zero values of coercivity up to room temperature (see inset in figure 4b). Figure S5 (in the SI) shows the ZFC-FC (zero field cooled-field cooled) measurements, which in view of the morphology of the nanocomposites, reflect the important dipolar and exchange interactions between the units forming them. Accordingly, the irreversibility between the ZFC and FC curve appears shifted to high temperatures ($T_{irrev} > 290$ K), which agrees with the fact that the nanoparticles in the nanocomposites appear in a blocked-like state, and consequently, have non-zero though small values of coercivity, despite the relatively large average diameter of the nanocomposites. Therefore, the nanocomposite magnetic response depends directly, not only on the type of magnetic material formed, but also on the size of the nanoparticles and interactions established in between, and also influenced by the processes occurring at the 3D interface.

In this regard, we can also consider the coupling between the two magnetic orders, the FiM and the AFM, by means of an exchange bias (EB) effect. This effect leads to an extra anisotropy contribution, such that the effective magnetic anisotropy energy of the composites can become larger than the thermal energy. In such a situation, the total magnetic moments of the hybrid nanocomposites are prevented from flipping over the energy barrier for all temperatures below T_N (Cr_2O_3) = 310 K, and thus the composites remain magnetically stable below this temperature. On the other hand, we must note down the fact that nanoparticles of the same material, grouped in nanocomposites, can be also magnetically stable in the same range of temperatures.[30] Accordingly, the system was cooled with no field applied (ZFC) and under an applied magnetic field (FC) of magnitude $H_{FC} = 20$ kOe. Figure 4c shows the hysteresis curves collected at 5 K (zero-field cooled (ZFC) and FC (20 kOe)) displaying a very small shift along the direction of the cooling field with coercivities $H_C=|H_{C1}-H_{C2}|/2 = 163$ Oe (ZFC) and $H_C=$ 198 Oe (FC) and exchange bias field $H_E= (H_{C1}+H_{C2})/2 = 17$ Oe (in the FC curve). The increase in coercivity and the small value of the exchange bias field H_E associated with the EB effect indicate uniaxial and unidirectional exchange anisotropies due to the exchange interaction between the uncompensated surface spins of Cr_2O_3 and the Fe_3O_4 in the nanocomposites.[31] The interfacial interaction between the magnetite and chromium oxide appears to be the main source of exchange bias, taking into account the exchange interaction that gives rise to magnetic order in the metal oxides. This interaction is often mediated through adjacent oxygen atoms and has a strong indirect exchange component that tends to favour an AFM alignment of the spins. Additionally, a second option can consider a spin-glass, given the nanoparticulated morphology of the nanocomposites.[32] On the other hand, though clear that there is an exchange interaction between the two oxides, not only because of the shift of the hysteresis loop after field cooling, but also because of the increase in coercivity, we can point out two main reasons for the very low value of exchange bias field H_E. First we can consider the fact of having a 3D interface between the two oxides, which averages out the exchange coupling and consequently the value of H_E, and second, we also have to take into account the postsynthetic metallic cation exchange at the interface between the two oxides, which can also decrease the value of H_E. Additionally, Fallarino *et al.* pointed out a limit in the magnetoelectric nature of the AFM Cr_2O_3 as decreasing size. As approaching this limit, the surface (boundary) magnetization can even dominate the magnetic response of otherwise antiferromagnetically ordered nanoparticles,[33] which can therefore minimize the AFM-FiM interaction required for the EB effect to happen.

Conclusions

In summary, we have presented a combination of techniques to characterize hybrid nanocomposites built up using magnetite and chromium oxide nanoparticles. While XRD and Raman spectroscopy prove successfully the combination of the ferrimagnetic magnetite and the magnetoelectric antiferromagnetic chromium oxide, SQUID magnetometry demonstrates the coupling in between. These hybrid nanocomposites set therefore an example of intriguing interfacial phenomena and illustrate the importance of the interface analysis in transition metal oxide heterostructures.

Notes and references

a Departamento de Física Aplicada, Universidade de Vigo, 36310 Vigo Spain; E-mail: vsalgue@uvigo.es
b Département Sciences et Analyses des Matériaux, CRP Gabriel Lippmann, 4422 Belvaux, Luxembourg.
c University of Luxembourg, 1511 Luxembourg, Luxembourg.
d Department of Physics, University of Warwick, Gibbet Hill Road, Coventry, CV4 7AL, UK.

† Electronic Supplementary Information (ESI) available: Figures S1. Raman spectra of the hybrid nanostructures as dried powder onto the sample holder, collected at room temperature and in three different spots of the sample using the 633 nm excitation wavelength. Figure S2 and S3 include the Raman spectrum of Cr_2O_3 nanoparticles and Fe_3O_4 nanocomposites, respectively. Figure S4 includes a comparison of MvsH hysteresis loops of nanocomposites of magnetite with and without chromium oxide. Figure S5 includes the temperature dependent magnetization (collected in ZFC-FC conditions) of the nanocomposites. See DOI: 10.1039/b000000x/

1. J. Maier. *Chem. Mater.* 2014, **26**, 348.
2. S. Kalinin, N. A. Spaldin. *Science* 2013, **341**, 858.
3. M. Palcut, K. Wiik, T. Grande. *J. Phys. Chem. C* 2007, **111**, 813.

4. B. J. Beberwyck, Y. Surendranth, A. P. Alivisatos. *J. Phys. Chem. C* 2013, **117**, 19759.
5. L. Carbone, P. D. Cozzoli. *Nano Today* 2010, **5**, 449.
6. E. Dagotto. *Science* 2007, **318**, 1076.
7. M. Bañobre-López, C. Vázquez, J. Rivas, M. A. López-Quintela. *Nanotechnology* 2003, **14**, 318.
8. X. Deng, X. Li, Q. Peng, X. Wang, J. Chen, Y. Li. *Angew. Chem. Int. Ed.* 2005, **44**, 2782.
9. J. F. Scott. *Rev. Mod. Phys*. 1974, **46**, 83.
10. D. L. A. de Faria, S. Venancio Silva, M. T. de Oliveira. *J. Raman Spectroscopy* 1997, **28**, 873.
11. M. N. Iliev, M. V. Abrashev, H. G. Lee, V. N. Popov, Y. Y. Sun, C. Thomsen, T. L. Meng, C. W. Chu. *J. Phys. Chem. of Solids* 1998, **59**, 1982.
12. O. N. Shebanova, P. Lazor. *J. Raman Spectroscopy* 2003, **34**, 845.
13. J. Kreisel, M. C. Weber, N. Dix, F. Sánchez, P. A. Thomas, J. Fontcuberta. *Advanced Functional Materials* 2012, **22**, 5044.
14. O. Chaix-Puchery, C. Cochard, P. Jadhav, J. Kreisel, N. Dix, F. Sánchez, J. Fontcuberta. *Appl. Phys. Lett.* 2011, **99**, 072901.
15. H. Zheng, J. Kreisel, Y.-H. Chu, R. Ramesh, L. Salamanca-Riba. *Applied Physics Letters* 2007, **90**, 113113.
16. F. Le Marrec, R. Farhi, M. El Marssi, J. L. Dellis, M. G. Karkut, D. Ariosa. *Physical Review B (Condensed Matter)* 2000, **61**, R6447.
17. T. Hart, R. Aggarwal, B. Lax. Ed. by M. Balkanski, Flammarion, Paris (1971).
18. T. Hart, S. B. Adams, H. Temkin. Ed. by Balkanski, M.; Leite R. C. C.; Porto, S. P. S. Wiley, New York (1975).
19. T. Hart, H. Temkin, S. B. Adams. Ed. by Balkanski, M.; Leite R. C. C.; Porto, S. P. S. Wiley, New York (1975).
20. K. F. McCarty, D. R. A. Boehme. *J. Solid State Chem.* 1989, **79**, 19.
21. A. B. Dávila-Ibáñez, N. J. Buurma, V. Salgueiriño. *Nanoscale* 2013, **5**, 4797.
22. S. Morup, D. E. Madsen, C. Frandsen, C. R. H. Bahl, M. F. Hansen. *J. Phys.: Condens. Matter* 2007, **19**, 213202.
23. C. R. H. Bahl, J. Garde, K. Lefmann, K.; T. B. S. Jensen, P.-A. Lingard, D.E. Madsen, S. Morup. *Eur. Phys. J. B* 2008, **62**, 53.
24. R. Mariño-Fernández, S. H. Masunaga, N. Fontaíña-Troitiño, M. P. Morales, J. Rivas, V. Salgueiriño. *J. Phys. Chem. C* 2011, **115**, 13991.
25. N. Fontaíña-Troitiño, S. Liébana-Viñas, B. Rodríguez-González, Z.-A. Li, M. Spasova, M. Farle, V. Salgueiriño. *Nano Letters* 2014, **14**, 640.
26. L. Néel. *C. R. Acad. Sci. Paris* 1961, **252**, 4075.
27. N. Wu, X. He, A. L. Wysocki, U. Lanke, T. Komesu, K. D. Belashchenko, C. Binek, P. A. Dowben. *Phys. Rev. Lett.* 2011, **106**, 087202.
28. X. He, Y. Wang, N. Wu, A. N. Caruso, E. Vescovo, K. D. Belashchenko, P. A. Dowben, C. Binek. *Nature Materials* 2010, **9**, 579.
29. J. Smit, H. P. H. Wijn. *Ferrites*. Philips Technical Library (1959).
30. S. Liébana-Viñas, R. Otero-Lorenzo, B. Rivas-Murias, V. Salgueiriño, *J. Phys.: Conf. Series* 2014, **521**, 012002.
31. J. Nogués, I. K. Schuller. *J. Magn. Magn. Mater.* 1999, **192**, 203.
32. V. Salgueiriño-Maceira, M. A. Correa-Duarte, M. Bañobre-López, M. Grzelczak, M. Farle, L. M. Liz-Marzan, J. Rivas. *Advanced Functional Materials* 2008, **18**, 616.
33. L. Fallarino, A. Berger, C. Binek. *Appl. Phys. Lett.*, 2014, **104**, 022403.